RSC
Applied Interfaces

ROYAL SOCIETY
OF CHEMISTRY

PAPER

View Article Online
View Journal

Check for updates

Cite this: DOI: 10.1039/d5lf00398a

Photo-deposition of Cu_2O on pre-annealed ZnO nanorods yields pn-type heterostructures with enhanced photocatalytic activity

Fredric G. Svensson,†[a] Erik Djurberg,[a] Yige Yan,[bc] Seohan Kim,[d] Jiri Henych,[ef] Jakub Tolasz,[e] Frederic Dappozze,[c] Stephane Parola,[b] Chantal Guillard,[c] Bozhidar I. Stefanov[g] and Lars Österlund*[h]

Received 21st December 2025,
Accepted 1st April 2026

DOI: 10.1039/d5lf00398a

rsc.li/RSCApplInter

Copper–zinc oxide pn-type heterostructures are promising visible-light-active photocatalysts because their intrinsic bandgaps and band alignment facilitate efficient charge separation. However, achieving controlled deposition of copper oxide nanoparticles on ZnO nanorods remains challenging, particularly in forming well-defined interfaces. Here, we report a UV-assisted photo-deposition method using $[Cu(EDTA)]^{2-}$ complexes to predominantly form Cu_2O nanoparticles on sea-urchin-like ZnO nanorods that either were used as-prepared or subjected to systematic post-heating treatments. The structural, chemical, and electronic properties of the resulting pn-type heterostructures were characterized by X-ray diffraction, electron microscopy, and photoelectron and photoluminescence spectroscopy, while phenol photodegradation products were quantified by HPLC. In contrast to the as-prepared ZnO nanorods, annealing treatment prior to Cu_2O deposition produces well-developed Cu_2O–ZnO interfaces, yielding pn-type heterostructures with enhanced photocatalytic degradation of phenol under UVA illumination. Our results indicate improved interfacial charge transfer, attributed to reduced lattice defects and removal of surface contaminants through annealing. These findings demonstrate that substrate surface preparation combined with atom-by-atom photo-deposition of chelated copper complexes provides a straightforward route for optimizing heterostructure catalysts with improved interfacial properties and enhanced photocatalytic activity.

1. Introduction

Heterogenous photocatalysis has been extensively investigated for the remediation of water contaminated with pollutants over the last decades.[1,2] Despite extensive search for new, efficient photocatalysts, in particular visible-light active photocatalysts, TiO_2 and ZnO remains the dominant metal oxides for environmental photocatalysis due to their high activity, availability and ease of preparation.[3] TiO_2 and ZnO are however wide bandgap metal oxide semiconductors and rely on UV illumination ($\lambda < 390$ nm) for electron–hole pair generation and subsequent radical formation (*e.g.* $O_2^{-\bullet}$, $OH^{-\bullet}$), which makes their application under solar light inefficient as only 5% of the solar radiation are energy-rich enough for bandgap illumination.[4]

Heterostructure catalysts can help overcome this limitation by combining appropriate constituent materials, but they introduce challenges in achieving efficient charge separation of excited electron–hole pairs and establishing good electronic contact across material interfaces. In assemblies of p-type and n-type nanoparticles, the formation of functional pn-type heterostructures differs fundamentally from that in epitaxially grown films, where smooth, parabolic band bending across a well-defined depletion region is established, enabling efficient charge separation *via* a strong built-in electric field. In contrast, a pn-type nanoparticle junction is typically formed by the physical contact of two pre-synthesized nanocrystals. The interface is a disordered, zero-dimensional point contact between curved surfaces with

---

[a] *Department of Materials Science and Engineering, The Ångström Laboratory, Uppsala University, Uppsala Box 35, 751 03, Sweden*
[b] *Laboratoire de Chimie, UMR 5182, ENS de Lyon, 69364 Lyon Cedex 07, France*
[c] *Institut de recherches sur la catalyse et l'environnement de Lyon (IRCELYON), UMR5256, CNRS – Université Lyon 1, 69626 Villeurbanne Cedex, France*
[d] *Yeongnam Regional Center, Korea Basic Science Institute, 46742, Rep Korea*
[e] *Materials Chemistry Department, Institute of Inorganic Chemistry of the Czech Academy of Sciences, 250 68 Husinec-Řež, Czechia*
[f] *Faculty of Environment, Jan Evangelista Purkyně University in Ústí nad Labem, Pasteurova 3632/15, 400 96 Ústí nad Labem, Czechia*
[g] *Department of Chemistry, Faculty of Electronic Engineering and Technologies, Technical University of Sofia, 8 Kliment Ohridski Blvd, 1756 Sofia, Bulgaria*
[h] *Department of Chemistry, Umeå University, 901 87 Umeå, Sweden. E-mail: lars.osterlund@umu.se*
† Present address: Department of Molecular Sciences, Swedish University of Agricultural Sciences, Box 7015, Uppsala 75007, Sweden.

misaligned crystal lattices. This structural imperfection, combined with the inherently high surface-to-volume ratio of nanoparticles, introduces a high density of mid-gap defect states. These states act as electron traps and pin the Fermi level at the interface. Consequently, band bending becomes localized, irregular, and inefficient with incompletely developed depletion regions, typically just the surface layers. Charge transfer across this junction often occurs *via* trap-assisted tunnelling or hopping leading to higher recombination losses. In photocatalytic processes, interfacial charge transfer—specifically, the transfer of excited electrons and holes from the particle surface to adsorbed oxygen and water/hydroxyl groups, respectively—is often the rate-limiting step for overall efficiency.[5] It is therefore desirable to develop methods to improve the interface structure in pn-heterostructure photocatalysts to allow built-in fields to develop and spatially separate the photo-excited electrons and holes.[6]

One of the most extensively studied pn-heterostructure systems for photocatalytic applications is Cu(I,II)O@ZnO,[7–9] where CuO (and Cu_2O) acts as the p-type semiconductor and ZnO as the n-type semiconductor. The Cu 3d–O 2p valence states of Cu_2O hybridize with the O 2p valence states of ZnO, because O 2p orbitals bridge both cations, forming separate bands that align and interact at the interface.[10] The conduction band edge of ZnO is lower than that of CuO, resulting in the flow of photo-excited electrons from CuO to ZnO, where $O^{2-\bullet}$ radicals are formed.[11] CuO@ZnO composites are reported to exhibit improved light absorption over the entire visible range compared to pure ZnO.[11–13] Holes in CuO react with water to form $OH^{\bullet}$ radicals.[14] However, preparing Cu(I,II)O/ZnO pn-heterostructures with well-developed interfaces remains challenging, as interfacial lattice imperfections and surface impurities introduce energy barriers that hinder charge transfer. In the case of ZnO, this is further challenged by the well-known deep bandgap states in ZnO nanoparticles.[15,16] Recently, elaborate metal–organic framework homojunction structures have been reported,[17] highlighting the importance of careful design to achieve well-defined junctions.

Several methods to prepare CuO@ZnO pn-heterostructures have been reported, including solid-state reactions between copper and zinc salts,[18] co-precipitation,[19] solution combustion,[20] and sol–gel methods.[8,21] The CuO@ZnO composites have been reported to exhibit 2–4 times better decomposition of pollutants during photocatalysis compared to the individual components.[7,13] There is also significant interest in well-defined CuO@ZnO nanocomposites due to their application in methanol synthesis.[22,23]

Recently, hydrothermally prepared, vertical ZnO rods were used as support to deposit Cu_2O by the advanced gas deposition method.[24] The resulting composite exhibited improved charge transfer, attributed to the high-quality interface achieved by vacuum deposition. As an alternative purely wet-chemical approach for *in situ* surface functionalization of photocatalysts with secondary phases for heterostructure formation, photo-deposition utilizes photogenerated charge carriers to directly reduce precursor metal ions to their metallic form or to deposit the corresponding metal oxides through reactions with photogenerated reactive oxygen species. Photo-deposition has been most widely applied to TiO_2 photocatalysts and is a well-understood process.[25,26]

Simple Cu(II) salts, such as aqueous cupric nitrate, are often directly used as Cu_xO precursors in photo-deposition electrolytes.[27,28] However, this approach limits the ability to tune reaction parameters—such as pH—which can influence the stoichiometry of the photo-deposited products, as illustrated by copper's Pourbaix diagram.[29,30] As a result, a mixture of the Cu^0, Cu_2O, and CuO phases is typically obtained. To improve control over the photo-deposition process, chelated Cu(II) species such as $[Cu(EDTA)]^{2-}$—commonly used in electroless plating—can be employed. These complexes are stable across a wide pH range. For instance, Venev *et al.*[31] reported on the wet-chemical photo-deposition of metallic copper on TiO_2, using $[Cu(EDTA)]^{2-}$ complex at pH 13, with formaldehyde as a reducing agent, to form conductive patterns on the TiO_2 surface. Follow-up studies using the same system demonstrated that at lower pH, a mixed Cu_2O/CuO oxide phase (in a 3 : 1 ratio) is deposited on the TiO_2 surface.[32] However, the photocatalytic performance of the functionalized TiO_2 catalysts was not addressed in either of these studies.

Although numerous studies have reported Cu_xO photo-deposition on TiO_2, this method is less frequently explored for ZnO—and seldom using chelated copper precursors.[30,33] Such an approach could be advantageous, as it allows for functionalization at near-neutral pH, thereby preventing ZnO dissolution caused by the acidic cupric nitrate solutions commonly used.

In the present study we apply post-heating of ZnO nanoparticles to remove mid-gap states to overcome Fermi level pinning. The photo-deposition of Cu atoms facilitates growth of Cu_2O bottom-up on the ZnO surface facilitating more developed oxide interface. We provide evidence that the resulting cleaner electronic interface enhances the driving force for charge separation, promoting direct band-to-band electron transfer from Cu_2O to ZnO, and reduces trap-mediated recombination.

2. Materials and methods

2.1 Materials

"Sea urchin"-like ZnO nanorods were prepared by a low-temperature method. Zinc acetate dihydrate (reagent grade, Sigma-Aldrich) (1.5 g) was dissolved in deionized (DI) water to a concentration of 0.27 M (25 mL). This was added to a 2.73 M (2.73 g) sodium hydroxide solution (25 mL), to give a reaction mixture with a total volume of 50 mL and final concentrations of Zn^{2+} and OH^- of 0.135 M and 1.37 M, respectively. The $Zn^{2+}:OH^-$ molar ratio was 1 : 10. The solution was heated at 50 °C in water for 90 min. After about 10 min, the solution turned slightly opaque, and after 90 min a massive precipitation of sea urchin-like ZnO had occurred. The precipitate was washed with DI water and centrifuged until the supernatant had reached neutral pH, to obtain the ZnO stock denoted as "as-prepared". The "post-heated" ZnO was prepared by annealing in air the as-prepared ZnO for 30 min at 500 °C in a furnace with 20 min temperature ramp.

Copper acetate monohydrate (98%, Aldrich) was dissolved in 25 mL DI H_2O and 1 equivalent of disodium EDTA (99%, Merck) dissolved in 25 mL DI H_2O was added. The final Cu^{2+} concentration was 0.1 M. The color changed from light blue to dark blue upon mixing, confirming complexation. The pH of this solution was about 3.8. The pH was then adjusted to 5.1 by dropwise addition of 1 M NaOH (99%, Merck). The $[Cu(EDTA)]^{2-}$ solution was stored in the dark at room temperature.

The photo-deposition followed a method adapted from ideas presented by Venev *et al.*;[31] 100 mg ZnO (post-heated or as-prepared) was placed in an 18 mL ceramic crucible together with an 8 mm Teflon-coated magnetic stirrer. Then, 1.5 mL of the $[Cu(EDTA)]^{2-}$ solution (Zn/Cu ratio of ~8 : 1) was added and stirred at 300 rpm. A UV source was placed 2.5 cm above the solution surface, and the reaction mixture was illuminated with a 365 nm LED light source (19 mW cm^{-2}, FWHM = 12 nm; Prizmatix Ltd., Holon, Israel) for 1 hour with stirring using a Teflon line magnet (400 rpm). The white powder turned brown-orange after the completed photo-deposition (see Fig. S1). The resulting Cu–Zn oxide composite was separated by centrifugation and washed with DI H_2O several times before air-dried under ambient conditions. The product powder remained brown-orange after washing with no apparent color shift over time. Cu_2O (99%, Aldrich) was used for preparation of physical Cu_2O/ZnO mixtures as reference samples. These were prepared by physically mixing the appropriate amounts of dry ZnO (as-prepared) and Cu_2O powders for a total weight of 100 mg, where 5 w% or 15 w% constitute Cu_2O.

2.2 X-ray diffraction

The as-prepared and post-heated ZnO was characterized by powder X-ray diffraction (PXRD). A Siemens D5000 powder X-ray diffractometer with Cu $K_{\alpha I,II}$ radiation (λ = 1.5418 Å) and Bragg–Brentano geometry was used. The step size was set to 0.02° and divergence- and anti-scattering slit widths of 1° were used. The Cu–Zn oxide composites were deposited on glass slides and analyzed by grazing incidence XRD (GIXRD) (Siemens D5000 diffractometer with Cu $K_{\alpha I,II}$ radiation (λ = 1.5418 Å) with the 0.03° step size and step time of 1 second). From the diffractograms, the average coherent crystallite sizes were estimated by the Scherrer equation, $D = K\lambda/(B_c \cos \theta)$, where D is the mean crystallite size, K is a shape factor (here 0.94), B_c is full width at half maximum (FWHM) corrected for instrumental broadening (NIST 1976 Al_2O_3 standard) and θ is the Bragg angle in radians. The average crystallite sizes for ZnO were from the FWHM of the (1 0 1) diffraction plane.

2.3 Electron microscopy

For morphological characterization and determination of elemental composition of the materials, a Zeiss LEO 1550 scanning electron microscope (SEM) equipped with a field emission gun (operated between 3 keV and 8 keV) and an Oxford Aztec energy dispersive X-ray spectroscopy (EDS) system was employed. All powder samples were dispersed on carbon tape for analysis.

Lattice spacing measured from selected area electron diffraction (SAED) were obtained using a field-emission transmission electron microscope (FE-TEM, JEOL, JEM-2100F). Phase identification was conducted with selected ZnO references from the PDF-5+ database suggested for ICDD 04-06-1673. For STEM-EDS analysis, a Thermo Fisher Scientific FEI Talos F200X scanning/transmission electron microscope equipped with a Super-X EDX detector system was used. The samples were deposited on a holey carbon grid from water suspension and air-dried before their inspection.

2.4 X-ray photoelectron spectroscopy

The oxidation states of copper were analyzed by X-ray photoelectron spectroscopy (XPS) employing a Quantera II Scanning XPS Microprobe (Physical Electronics) equipped with an Al K_α source. A low-energy flood-gun operating at 1.0 V and 20.0 μA beam current was used for charge compensation. For the survey spectra, a pass energy of 224 eV and a resolution of 0.8 eV was used, and for high-resolution spectra a pass energy of 55 eV and 0.1 eV resolution were used. The spectra were calibrated against the 284.8 eV peak due to adventitious carbon. To investigate possible oxidation of Cu during photocatalysis, high resolution XPS of Cu and O were recorded before and after photocatalytic degradation of phenol.

2.5 Surface area measurements

A Micromeritics ASAP 2020 instrument was used to determine the surface areas of the two different Cu_2O@ZnO pn-type heterostructure catalysts by means of BET analysis. The samples were pre-dried in a furnace at 120 °C for 2 h, then stored in sealed plastic vessels in a desiccator before degassing under vacuum at 120 °C for 2 h prior to analysis.

2.6 Photoluminescence spectroscopy

Photoluminescence spectroscopy (PL) was used to measure the near bandgap emission and deep level emission of the investigated samples. An Edinburgh Instrument FLS1000 equipped with a halogen lamp employing 360 nm emission wavelength was used to collect emission spectra at room temperature on drop casted powder samples dispersed in ethanol on quartz substrates. Triplicate scan spectra were acquired with a 1 nm step size and 0.1 s dwell time in the range of 360 nm to 825 nm. The presented deep level emission bands were normalized against the integrated near-band emission (NBE) ZnO line for each spectrum occurring at 368 nm (3.37 eV), which we assume is not affected by Cu photo-deposition.

2.7 Photocatalytic degradation of phenol

Photocatalytic degradation tests were conducted by using a 100 mL Pyrex photo-reactor in an air atmosphere. Phenol (99%, Sigma-Aldrich) was employed as a model-pollutant. For all the experiments, the concentration of the photocatalyst was set to 1 g L^{-1}. In detail, 100 mg of the catalyst was added to 100 mL of a solution of the pollutant (60 ppm) with top motorized stirring for 60 min in the dark to reach equilibrium. A pre-heated UV-A PL-L 18W (Philips) was positioned under the reactor. The irradiation at 365 nm measured on the inner bottom side of the reactor was 4.8 mW cm^{-2}. 0.8 mL of the solution was sampled and filtrated on a MILLEX HVLP 0.45 μm hydrophilic filter (Millipore, Burlington, MA, USA) for the HPLC analyses.

HPLC analyses for phenol was performed using a Shimadzu system (Shimadzu, Japan) equipped with a photodiode array detector and a 150 mm × 4.6 mm × 2.7 μm-Ascentis Express 90 Å AQ-C18 column (Supelco Merck). The mobile phase was a 95% v/5% v acidified water (with 0.1% w/w HCOOH)/methanol mixed solution. The flow rate was set at 1.0 mL min^{-1}. The column working temperature was set at 40 °C.

3. Results and discussion

3.1 Structure and morphology

Fig. 1 shows the indexed X-ray diffraction (XRD) diffractograms of the Cu–Zn oxide samples using grazing incidence XRD (GIXRD). Despite a noticeable change from white to pale orange-brown color on the Cu-deposited Zn oxide samples, the crystalline phases other than ZnO could not be detected by Bragg–Brentano geometry. The average crystallite sizes for the as-prepared and post-heated ZnO were 41.8 nm and 55.9 nm, respectively, as determined by Scherrer analysis. From GIXRD, several copper oxide related phases could be detected, mainly Cu_2O (cubic, space group $Pn\bar{3}m$), and minority CuO (monoclinic, space group $C2/c$) and metallic copper (cubic, space group $Fm\bar{3}m$) diffraction peaks, which are in good agreement with the XPS results below. We therefore denote the heterostructures "Cu_2O@ZnO" as the majority copper oxide phase is Cu_2O. Crystallite size was determined by Scherrer analysis of the FWHM of XRD reflections after correcting for instrumental broadening. The crystallite sizes for Cu_2O were estimated to be 16.6 nm and 23.7 nm for Cu_2O@ZnO (as-prepared) and Cu_2O@ZnO (post-heated), respectively, using Scherrer calculation. The average crystallite sizes for metallic Cu were 15.0 nm and 20.1 nm for Cu_2O@ZnO (as-prepared) and Cu_2O@ZnO (post-heated), respectively, showing consistently that the crystallites grow larger on the post-heated material. We interpret this as the larger mobility of the Cu species on post-heated ZnO due to the reduced number of nucleation sites on the surface. A digital photograph of the Cu_2O@ZnO powder is shown in Fig. S2. Moderate stirring (300 rpm) was required as only the solution-exposed part of the ZnO would be deposited otherwise. The specific surface areas for Cu_2O@ZnO (as-prepared) and Cu_2O@ZnO (post-heated) were determined to be 11.7 ± 0.2 m^2 g^{-1} and 7.8 ± 0.4 m^2 g^{-1}, respectively.

Fig. 2 shows the SEM images of Cu deposited on post-heated ZnO, exhibiting sea urchin-like structures with diameters between 2 μm to 5 μm. The sea urchin-like structures were intact after the Cu photo-deposition synthesis step. No evident observable changes in morphology were seen for the as-prepared ZnO (Fig. S3). As evident from the elemental maps in Fig. 2, copper appears to be evenly distributed over the ZnO samples, which is also confirmed by

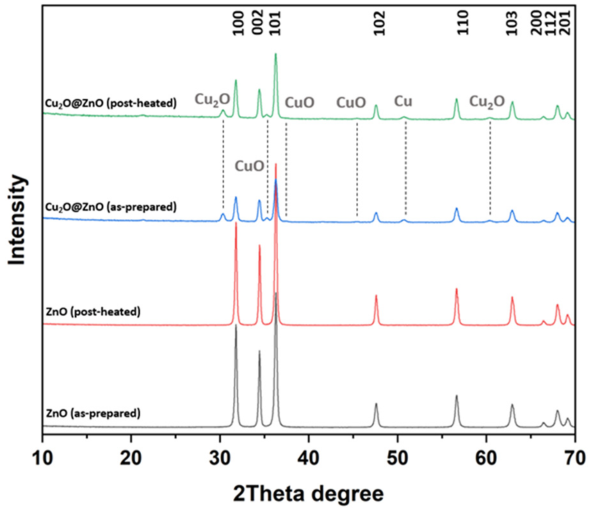

Fig. 1 Indexed diffraction patterns for the four photocatalysts labelled at each diffractogram. The ZnO patterns correspond to the reference pattern for the wurtzite phase (ICCD #04-006-1673). The copper-related patterns were indexed as metallic Cu (ICCD #04-001-3178), Cu_2O (ICCD #04-006-6514), and CuO (ICCD #00-048-1548).

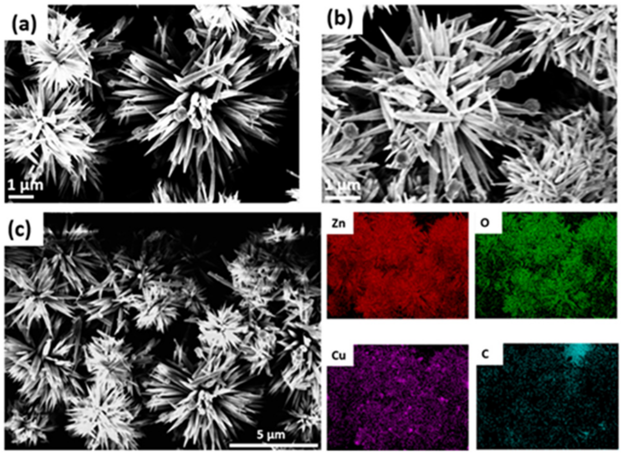

Fig. 2 (a and b) Representative SEM micrographs of Cu_2O@ZnO deposited on post-heated ZnO. (c) Cluster Cu_2O@ZnO deposited on post-heated ZnO with elemental mapping, confirming the presence of zinc, oxygen, and copper. About 50 copper spheres can be seen in Fig. 2c.

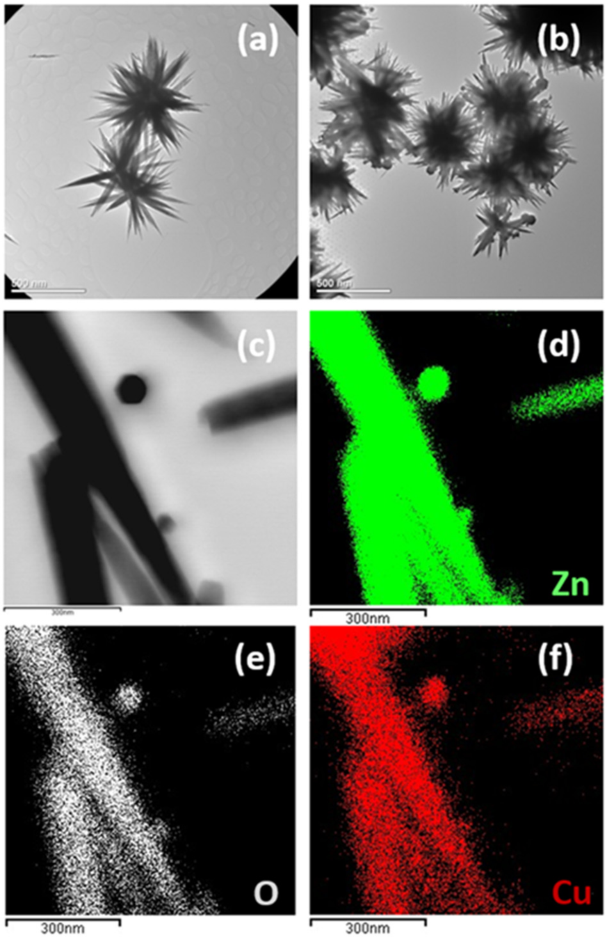

Fig. 3 TEM micrographs of (a) ZnO post-heated, and (b and c) $Cu_2O@ZnO$ (post-heated). (d–f) EDS analyses of $Cu_2O@ZnO$, confirming the presence of Zn, O, and Cu, respectively.

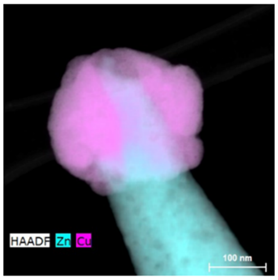

Fig. 4 High-resolution STEM-EDS micrograph of the tip of a ZnO rod (blue) with copper and copper oxide grown on the tip (purple).

TEM analysis showing homogenous deposition of nano copper containing particles over the ZnO rods (Fig. 3). Detailed analysis of the SEM images show that the $Cu_2O@ZnO$ samples consist of small particles decorating the ZnO rods, and larger, about 100 nm, aggregates of smaller copper oxide nanoparticles spheres that according to the elemental analysis mainly consist of copper in different oxidation states, as elaborated in the XPS section below (Fig. 3). TEM shows that these particles mainly exist at the tips of the ZnO rods (Fig. 3b), suggesting that these are sites for nucleation of excess Cu. High-resolution STEM-EDS confirms that these spheres consist of Cu and Cu_2O (Fig. 4).

A tentative explanation for this may be that the alternating positive and negative planes within the wurtzite structure causes an internal electric field, which promotes the separation of the photo-excited electron–hole pair. Electrons migrate towards the positive (001) plane where reduction reactions may occur.[34] It might then be possible that an increased concentration of electrons at the ZnO tips facilitates reduction and nucleation of metallic Cu and Cu_2O, causing the formation of observed spheres, thus providing an explanation for the weak metallic Cu peaks in XRD seen in Fig. 1. The formation of Au nanoparticle spheres on the tips of CdSe and CdSe/CdS nanorods under illumination has been reported.[35] It is known that direct electrical pathways provided by ZnO nanowires facilitate rapid collection of carriers that are formed throughout connect wires.[36] The sea urchin-like structures seen in Fig. 2 may thus expose a higher effective surface for photo-induced redox surface reactions than the directly illuminated fraction of the sample.

3.2 Chemical composition

Fig. 5 shows the high-resolution spectra of $Cu_2O@ZnO$ samples before and after photocatalytic degradation of

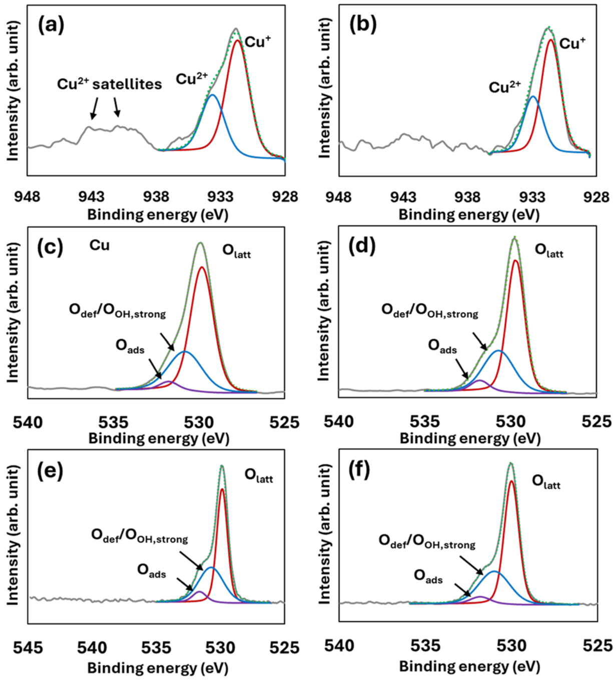

Fig. 5 High resolution XPS spectra of $Cu_2O@ZnO$ (post-heated) and ZnO (as-prepared and post-heated). Cu $2p_{3/2}$ of $Cu_2O@ZnO$ before (a) and after (b) photocatalysis. O 1s spectra of $Cu_2O@ZnO$ before (c) and after (d) photocatalysis. O 1s spectra of ZnO (as-prepared) (e) and ZnO (post-heated at 500 °C for 30 min) (f). The deconvoluted contributions of Cu^+ and Cu^{2+} are indicated. The O 1s spectra due to $Cu^{2+}–O_{ads}/O_{def/OH\text{-}strong}$ and $Zn–O_{ads}/O_{def/OH\text{-}strong}$ overlap and are represented by one band each.

phenol. Survey spectra are presented in Fig. S4a and b, while binding energies and elemental composition are shown in Table S1. Here we focus the analysis of the Cu-complexes deposited on post-heated ZnO. The electron binding energies of metallic copper and Cu^{1+} (as in Cu_2O) are overlapping and not easily separated. In contrast, the Cu^{1+} and Cu^{2+} (in Cu_2O and CuO) positions are separated by about 1.3 eV.[37] Deconvoluting the high-resolution spectrum for samples before photocatalysis for Cu $2p_{3/2}$ (Fig. 5a) results in two major components centred at 931.6 eV and 933.6 eV, which corresponds to Cu^+ and Cu^{2+}, respectively. Quantifying their relative intensities from the integrated area shows an approximate Cu^+ to Cu^{2+} ratio of about 2 : 1. It is however expected that Cu–OH contributes above 934 eV, which also can be discerned in Fig. 5, and contribute to the Cu^{2+} band, and thus lower the Cu^{2+} contribution. The distinction between $Cu^{2+}–(OH)_2$ and $Cu^{2+}–O$ is however difficult in XPS and was not attempted here due to large S/N in the Cu 2p spectra. For the samples analysed before the photocatalysis experiments, the two characteristic Cu^{2+} satellites can be observed between 940 eV and 945 eV (Fig. 5a). These satellites are found for Cu^{2+} (as in CuO) and confirm the presence of a CuO phase. XPS is however expected to show larger amounts of CuO than inferred from the XRD data since it is a surface-sensitive technique due to the oxidation of the outermost Cu deposition to CuO in the oxidizing environment, which is not representative for the deeper Cu–Zn oxide interface. After photocatalysis (Fig. 5c) the Cu^{2+} satellite peaks decreased while the integrated areas Cu^{2+}:Cu^+ remained approximately the same, again suggesting that Cu–OH contributes to the deconvoluted Cu^{2+} band. The peak for the $2p_{3/2}$ peak at 931.5 eV did not change much. A previous study on the photodecomposition of $[Cu(EDTA)]^{2-}$ over TiO_2 also found metallic Cu and Cu_2O depositions over the TiO_2.[38]

To get further insight into the chemistry of the mixed oxide, the O 1s peak was analyzed. Based on the high copper coverage from SEM-EDS and TEM-EDS analysis, along with the short penetration depth of XPS, it is reasonable to assume that both Cu and Zn oxides contribute to the O 1s signal. The O 1s positions of Cu^+ and Cu^{2+} differ slightly and can provide further information about the different oxide phases. It has been reported that the component at ∼530 eV represents O in Cu_2O, and the higher binding energy (∼530.6 eV) is O in CuO.[40] In addition, surface OH due to both Zn and Cu is expected to contribute to the O 1s spectra, where the component at ∼531.8 eV represents Zn–OH/Cu–OH.[41] Furthermore, the as-prepared ZnO was previously determined to have more surface hydroxyls compared to post-heated ZnO,[39] and it is reasonable that surface OH are replenished upon photocatalysis. Fig. 5c and d show O 1s spectra before and after photocatalysis, respectively. The O 1s shift was deconvoluted into three components due to lattice oxygen (O^{2-} in metal oxide), defect-associated oxygen and/or strongly bound surface hydroxyls, and adsorbed oxygen species (*e.g.*, weakly bound OH, H_2O, carbonates, organics), with binding energies at 529.8 eV, 530.8 eV, and 531.8 eV, respectively (Fig. 5c). The O 1s binding energies remained approximately the same after photocatalysis. Before photocatalysis, the Cu^+, Cu^{2+}, and Zn–OH/Cu–OH distribution is ≈66 at%, ≈30at%, and ≈3 at%, respectively, and after photocatalysis ≈62 at%, ≈33 at%, and ≈5 at%, respectively, showing slight surface oxidation of the Cu oxide during photocatalysis. In comparison, pure ZnO (as-prepared) and ZnO (post-heated at 500 °C for 30 min) from our previous work[39] contained 6 at% and 5 at% Zn–OH, respectively (Fig. 5e and f), indicating that surface hydroxyls and defect-associated oxygen are depleted during photo-deposition of Cu, and gradually formed during photocatalysis. As discussed below, surface OH contributes to the initial phenol photodegradation and thus affects the comparison between ZnO and Cu_2O@ZnO samples. Finally, it should be noted that due to the very small shifts of $Cu^{2+}–O_{ads}/O_{def/OH\text{-}strong}$ and $Zn–O_{ads}/O_{def/OH\text{-}strong}$, deconvoluting their separate contributions is very difficult and are therefore here presented as the combined contribution.

3.3 Electronic structure and interfacial charge transfer

It is evident that post-heating the samples for 30 min at 500 °C almost completely removes the deepest emission band at about 620 nm regardless of whether Cu_2O is photo-deposited on the ZnO rods, or not. Photo-deposition of the as-prepared ZnO with Cu_2O nanoparticles (Cu_2O@ZnO-as-prepared) quenches the 620 nm emission band, although not eliminating it. A new emission line at about 718 nm appears on post-heated ZnO with deposited Cu_2O nanoparticles (Cu_2O@ZnO-post-heated), which is not clearly resolved for the Cu_2O@ZnO-as-prepared sample. Emission bands due to excitons are not observed at room temperature,[42] and there are no observable bands in the 430 nm to 470 nm region, which have been attributed to surface states, adsorbates, or small metallic Cu clusters.[43] No emission due to Cu_2O was observed in any of the samples (expected to occur around 600 nm), indicating efficient quenching of interband decay within Cu_2O. The latter is augmented by the indirect-like optical properties of Cu_2O due the dipole-forbidden nature of the optical transition at the Γ point. Comparing with previously reported data on the band edge and Fermi level position for Cu_2O@ZnO heterostructures,[24,44] we therefore attribute the 718 nm emission to the interfacial radiative recombination across the Cu_2O/ZnO heterostructure. Electrons from the ZnO conduction band recombine with holes in the Cu_2O valence band, giving a lower-energy emission that is not present in pure ZnO. The 718 nm emission (about 1.73 eV) is below the Cu_2O bandgap, consistent with type-II band alignment interfacial recombination.

We note that quenching of the deep level emission band after post-heating ZnO nanorods correlates with the disappearance of OH and hydride species bonded to lattice defects (O vacancies and Zn interstitials) as ZnO becomes more crystalline and defects are healed upon annealing.[39] The disappearance of those defects has been shown to decrease the initial rate of photocatalytic degradation of phenol due to loss of OH radicals generated from these sites.[39] As we show in the next section, Cu_2O@ZnO can therefore not *per se* be expected to promote phenol photodegradation if those sites are blocked by Cu_2O nanoparticles. Hence, a trade-off is apparent. While post-heating ZnO yields Cu_2O@ZnO with improved electronic coupling across the Cu_2O/ZnO interfaces, Cu_2O deposition and post-heating block and reduce photocatalytic active OH and hydride species. In the next section, we quantify these counteracting effects.

3.4 Photocatalytic degradation of phenol

To qualitatively validate the hypothesis of improved electron–hole pair separation due to charge transfer across pn-junctions, the photocatalytic degradation of an aqueous phenol solution (60 ppm) under UVA illumination was studied over a period of three hours. Phenol was chosen as the model organic compound since the decomposition chemistry and intermediate steps are well-known and can be accurately measured. The decomposition was followed by HPLC-PDA. It was found that the post-heated ZnO and Cu_2O@ZnO degraded phenol much faster compared to the as-prepared ZnO and Cu_2O@ZnO samples. After 3 hours of UV illumination, the as-prepared ZnO, as-prepared Cu_2O@ZnO, post-heated ZnO, and post-heated Cu_2O@ZnO showed 17.8%, 25.5%, 38.7%, and 48.3% degradation of the initial phenol, respectively (Fig. 7). The concentration of phenol as a function of illumination time and corresponding pseudo-first order plots are shown in Fig. 8. The corresponding degradation rate constants are presented in Table 1. It is seen that the post-heated ZnO and Cu_2O@ZnO catalysts yield markedly higher rates compared to those based on the as-prepared ZnO. Phenol without any catalyst did not show any degradation under UV-illumination. The effect of only Cu_2O and physical mixtures of Cu_2O with ZnO (as-prepared) at two different concentrations (5 weight% and 15 weight% Cu_2O) were also investigated (Fig. S5). Cu_2O had very low photocatalytic activity, with 95% of phenol remaining after 180 min of UV illumination. The physical mixture Cu_2O/ZnO (as-prepared) with 5 w% and 15 wt% Cu_2O showed 17.4% and 21.6% phenol degradation over 180 min. Thus, simple physical mixing of Cu_2O and ZnO gives marginally better decomposition than the as-prepared ZnO, but less than Cu_2O@ZnO (as-prepared). It is seen in Fig. S5 that the physical addition of 5 wt% or 15 wt% Cu_2O differs little in degradation. Hence, we conclude that attachment of Cu_2O on ZnO by photo-deposition enhances the photocatalytic activity. It is evident by comparing Fig. 8 and S5 that the post-heated Cu_2O/ZnO heterostructure gives much higher photodegradation activity than what can be explained by the constituent materials, but that the as-prepared photo-deposited Cu_2O/ZnO only has slightly higher activity (25.5%). It is further seen that an increased Cu_2O loading in the physical ZnO and Cu_2O mixtures increases the phenol degradation activity, but even with a Cu_2O loading much larger than what we estimate on the photo-deposited Cu_2O/ZnO samples (15 wt% Cu_2O), the phenol degradation is still lower than what is observed on the "as-prepared" photo-deposited Cu_2O/ZnO. These observations indicate that the pn-heterostructures deposited on defect-rich and contaminated ZnO surfaces (from synthesis residues and non-perfect crystallization) suffer from poor electrical contact (poor interfacial bonding), but that photo-deposition of the Cu precursor directly on the ZnO surface improves interfacial bonding (the atom-by-atom method to build pn-heterostructure). In contrast, performing photo-deposition on a post-heated ZnO surface, where midgap states to some extents have been healed, significantly improves the phenol photodegradation performance (48.3% degradation).

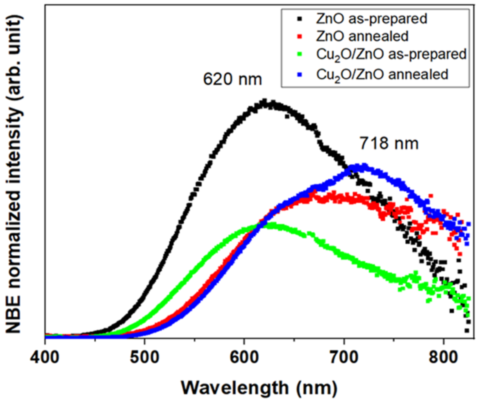

Fig. 6 Near-band edge (NBE) normalized photoluminescence spectra of the as-prepared annealed ZnO nanorods, and corresponding spectra of Cu_2O@ZnO, showing deep level emission states.

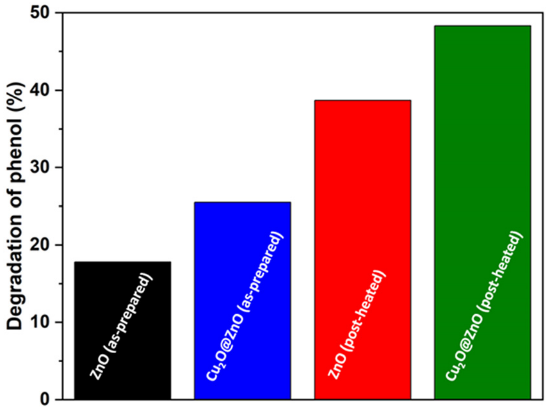

Fig. 7 Percent degradation of phenol by the four different photocatalysts after 3 hours of UV-A illumination.

Previous work has also shown the beneficial photodegradation activity of CuO/ZnO and Cu_2O/ZnO heterostructures, although this work has not quantified the influence of interfacial properties. Wang *et al.*[45] prepared ZnO whiskers decorated with CuO particles by a photodeposition method. They observed much improved photocatalytic decomposition of methyl orange from the

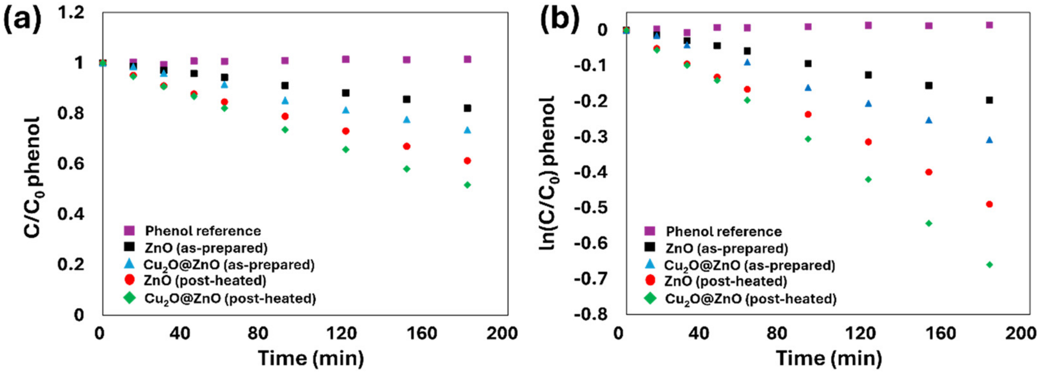

Fig. 8 (a) Normalized phenol concentration as a function of UVA illumination (365 nm). (b) Pseudo first-order plot for phenol removal. The initial phenol concentration was 60 ppm and the photocatalyst concentration was 1 g L^{-1} in all experiments. The control experiment with no photocatalyst is denoted "phenol reference".

Table 1 Summary of the photocatalytic studies. Rate constants for phenol degradation and the formation of the catechol and hydroquinone intermediates, normalized for surface area, are reported

Sample	Phenol decomposition rate (min^{-1})	Phenol decomposition rate (μmole per min m^{-2})	Catechol formation rate (μmole per min m^{-2})	Hydroquinone formation rate (μmole per min m^{-2})	Specific surface area (g m^{-2})
ZnO as-prepared	0.0011	0.094	0.03	0.03	7.1 ± 0.2
ZnO post-heated	0.0017	0.22	0.05	0.07	6.1 ± 0.2
Cu$_2$O@ZnO as-prepared	0.0026	0.086	0.02	0.02	11.7 ± 0.2
Cu$_2$O@ZnO post-heated	0.0037	0.23	0.04	0.06	7.8 ± 0.4

photo of the composite compared to physical mixtures of ZnO and CuO. However, they reported that too high deposition of CuO decreased the photocatalytic activity. Mahrsi and co-workers prepared Cu$_2$O/CuO@ZnO composites by photo-deposition of Cu(NO$_3$)$_2$ over ZnO nanorods.[46] The composites were found to be more effective in the photocatalytic decomposition of rhodamine B and remazol brilliant blue R compared to only ZnO rods. They also noticed that increasing copper loading decreased the photocatalytic activity.

The formation of the intermediate compounds catechol and hydroquinone was clearly observed (Fig. 9a and b). No other intermediates were detected under our experimental conditions. These species are primary degradation products of phenol resulting from attack by OH and O$_2$ radicals, which abstract delocalized π-electrons from the aromatic ring, and initiates ring opening and subsequent formation of carboxylates (acetate and formate; RCOO), whose anions can bind to the catalyst, as follows:[47]

$$\text{Phenol} \xrightarrow{^{\cdot}\text{OH}} \left\{\begin{array}{l}\text{catechol}\\ \text{hydroquinone}\end{array}\right. \xrightarrow{\text{oxidation}} \text{benzoquinone} \xrightarrow{\text{ring opening}} \ldots$$
$$\rightarrow \text{carboxylic acids} \rightarrow CO_2 + H_2O$$

At the start (0 min), neither catechol nor hydroquinone was detected. However, as the UV-illumination proceeded, both intermediates started to form. The formation of intermediates was highest for post-heated ZnO and Cu$_2$O@ZnO catalysts. The photodegradation rate of phenol was also higher on post-heated ZnO-based samples, 1.5 times higher for post-heated ZnO and 1.4 times for post-heated Cu$_2$O@ZnO.

It is well-established that photo-deposition products tend to localize at regions where photogenerated electrons or holes accumulate, such as specific crystal facets or surface defects like oxygen vacancies. Therefore, an additional consideration is the influence of the surface state, defect density, and crystallinity on the photo-deposition process. While defective surfaces generally are reported to enhance photocatalytic activity on ZnO,[39] they may be less favourable for photo-deposition functionalization since they act as traps for excitons.[48]

Comparing the phenol photo-degradation rate for post-heated ZnO and Cu$_2$O@ZnO-post-heated catalysts, we see that the normalized rate is only slightly higher for the Cu$_2$O@ZnO pn-type heterostructure catalysts, while it is significantly higher than the corresponding Cu$_2$O@ZnO prepared from the as-prepared ZnO nanorods (by a factor of almost 3). The Cu$_2$O@ZnO catalyst prepared from the as-prepared ZnO nanorods shows the lowest activity of all catalysts studied. These results can be rationalized as follows. Previous photocatalytic photo-oxidation studies have shown that surface defects and hydroxyls play an important role in nanostructured ZnO photocatalysts.[49] Loss of reactive hydroxyls during heating of ZnO lead to reduced activity (which is *e.g.* evident in the loss of Zn–OH deduced from the O 1s spectra in XPS).[39,50] The data

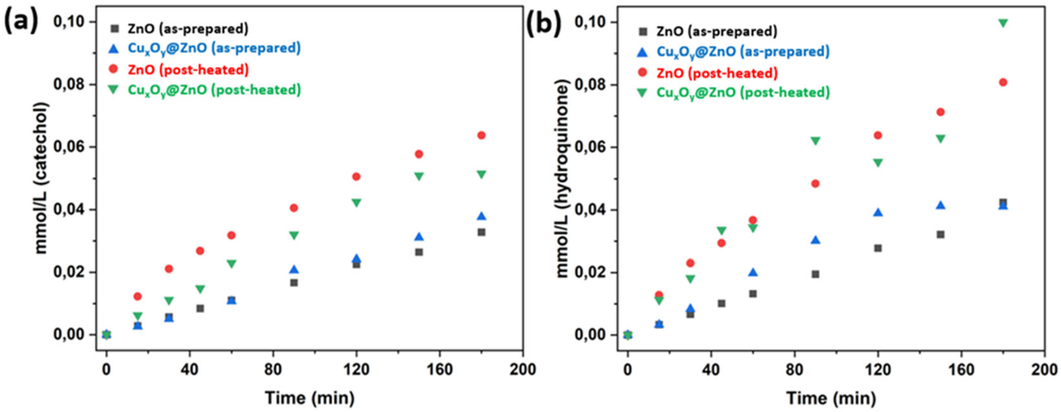

Fig. 9 (a) Formation of catechol during the decomposition of phenol. (b) Formation of hydroquinone during the decomposition of phenol.

shown in Fig. 6 shows that the deep level emission band in ZnO quenched upon post-heating, which we attribute to the removal of active OH and hydride species at defective ZnO lattice sites. This conclusion apparently contradicts the observation that the phenol degradation rate is about 1.5 times higher after post-heating ZnO. However, the detrimental effect of synthesis impurity site-blocking dominates the reactivity on the as-prepared ZnO, as we previously have reported on ZnO synthesised by the same methods.[39]

It is observed that the first hydroxylation step is larger on the post-heated ZnO than the post-heated Cu_2O@ZnO, which qualitatively support that the defective ZnO sites (primarily O vacancies) are responsible for the high activity on the former photocatalyst due to the larger abundance of these sites (since Cu_2O blocks some of these sites).

These sites are gradually consumed and are not catalytic. In contrast, the reaction rate for subsequent steps is faster on the post-heated Cu_2O@ZnO, which we argue is due to the catalytic generation of radicals at the Cu_2O/ZnO interface where interfacial charge transfer is enhanced (as inferred from Fig. 6). Hence, the mechanism for photodecomposition is different on the ZnO and Cu_2O@ZnO photocatalysts and they expose different active sites for phenol photodecomposition: reactive hydroxyls on ZnO and enhanced radical generation on the post-heated Cu_2O@ZnO. The observed differences between the two Cu_2O@ZnO catalysts can be explained by their different interfacial structure and a more developed electronic interaction between Cu_2O and ZnO in the samples prepared using post-heated ZnO. These features are consistent with enhanced electron–hole pair separation in the latter, which correlates with improved performance of the resulting pn-heterojunction photocatalyst.

4. Conclusions

In this work we have presented a simple wet chemical method to prepare Cu_2O@ZnO oxide pn-type heterostructure catalysts by employing photo-deposition of a $[Cu(EDTA)]^{2-}$ complex over ZnO sea urchin-like structures. This method yielded simultaneous deposition of Cu homogenously distributed over the ZnO structures with possible excess Cu forming larger clusters at the tips of the ZnO nanorods. The Cu_2O@ZnO pn-heterojunction prepared on pre-heated ZnO showed higher efficiency (1.4 times) for photodegradation of phenol compared to the catalyst prepared on the as-prepared ZnO, degrading 48.3% of phenol after 180 minutes of UV-illumination. The ZnO post-heating step results in ZnO with well-developed facets and reduced amount of organic surface contaminants leading to better contact between the ZnO and Cu_2O phases, which may improve electron–hole separation of photo-excited electron–hole pairs across their interfaces. Our work highlights the importance of employing well-crystallized materials with minimal surface impurities to achieve good interfacial bonding to improve interfacial charge transfer when preparing pn-type heterostructure catalysts by wet chemical methods.

Author contributions

FGS – formal analysis, investigation, methodology, validation, visualization, writing – original draft, review & editing; ED – formal analysis and investigation; YY – formal analysis, investigation, writing – review & editing; SK – investigation, writing – review & editing; JH – writing – formal analysis, review & editing; JT – investigation and formal analysis; FD – investigation, writing – review & editing; SP – supervision, writing – review & editing; CG – writing – supervision, review & editing; BIS – methodology, writing – review & editing; LÖ – conceptualization, formal analysis, funding acquisition, methodology, project administration, resources, supervision, validation, visualization, writing – original draft, review & editing.

Conflicts of interest

There are no conflicts to declare.

Data availability

The data supporting this article have been included as part of the supplementary information (SI).

Supplementary information is available. See DOI: https://doi.org/10.1039/d5lf00398a.

Acknowledgements

The authors would like to thank the European Commisson Horizon under the 2020 Framework Programme and the Swedish Research Agency Formas for the funding (grant no. 2020-03196), in the frame of the collaborative international consortium GreenWaterTech, financed under the ERA-NET AquaticPollutants Joint Transnational Call (869178-AquaticPollutants). This ERA-NET is an integral part of the activities developed by the Water, Oceans, and AMR Joint Programming Initiatives. B. I. S. is grateful to BNSF project KP-06-N-59/11.

Notes and references

1 R. Suresh, L. Gnanasekaran, S. Rajendran, M. Soto-Moscoso, W. H. Chen, P. L. Show and K. S. Khoo, *Environ. Sci. Technol.*, 2023, **31**, 103149.

2 A. S. Morshedy, E. M. El-Fawal, T. Zaki, A. A. El-Zahhar, M. M. Alghamdi and A. M. A. El Naggar, *Inorg. Chem. Commun.*, 2024, **163**, 112307.

3 H. Al-Mohamadi, S. A. Awad, A. K. Sharma, N. Fayzullaev, A. Tavara-Aponte, L. Chiguala-Contreras, A. Amari, B. C. Rodrigues, M. A. Tahoon and H. Esmaeili, *Catalysts*, 2024, **14**, 420.

4 S. Madronich, in *Environmental UV Photobiology*, ed. A. R. Young, J. Moan, L. O. Björn and W. Nultsch, Springer, New York, 1993.

5 W. Y. Teoh, J. A. Scott and R. Amal, *J. Phys. Chem. Lett.*, 2012, **3**, 629–639.

6 R. Mishra, S. Bera, R. Chatterjee, S. Banerjee, S. Bhattacharya, A. Biwas, S. Mallick and S. Roy, *Appl. Surf. Sci. Adv.*, 2022, **9**, 100241.

7 S. Das and V. C. Srivastava, *Nanotechnol. Rev.*, 2018, **7**, 267–282.

8 J. X. Liu, H. Wang, H. Wu, Y. Yang, C. Wang, Q. Wang, B. Jia and J. Zheng, *J. Mater. Chem. A*, 2024, **12**, 20838.

9 S. Sun, *Nanoscale*, 2015, **7**, 10850.

10 R. Marschall, *Adv. Funct. Mater.*, 2014, **24**, 2421–2440.

11 K. Luo, W. Hu, J. Wei, Q. Zhang, Z. Wu, D. Li, F. Miao, Y. Huang, M. Xu, J. Ma, C. Li, G. Chen, R. Han, X. L. Wang, X. Cui and P. Ruterana, *Phys. Chem. Chem. Phys.*, 2021, **23**, 10768.

12 Y. Wang, S. Li, H. Shi and K. Yu, *Nanoscale*, 2012, **4**, 7817.

13 L. Zhu, H. Li, Z. Liu, Y. Xie and D. Xiong, *J. Phys. Chem. C*, 2018, **122**, 9531–9539.

14 A. Dastider, H. Saha, M. J. F. Anik, M. Jamal and M. M. Billah, *RCS Adv.*, 2024, **14**, 11677–11693.

15 U. Özgur, Y. I. Alivov, C. Liu, A. Teke, M. A. Reshchikov, S. Dogan, V. Avrutin, S. J. Cho and H. Morkoc, *J. Appl. Phys.*, 2005, **98**, 041301.

16 S. B. Zhang, S. H. Wei and A. Zunger, *Phys. Rev. B: Condens. Matter Mater. Phys.*, 2001, **63**, 075205.

17 Y. Liu, C. Chen, J. Valdez, D. M. Meira, W. He, Y. Wang, C. Harnagea, Q. Lu, T. Guner, H. Wang, C. H. Liu, Q. Zhang, S. Huang, A. Yurtsever, M. Chaker and D. Ma, *Nat. Commun.*, 2021, **12**, 1231.

18 R. Saravanan, S. Karthikayan, V. K. Gupta, G. Sekaran, V. Narayanan and A. Stephen, *Mater. Sci. Eng., C*, 2013, **33**, 91–98.

19 B. Li and Y. Wang, *Superlattices Microstruct.*, 2010, **47**, 615–623.

20 B. Abebe, D. Tsegaye, C. Sori, R. C. K. R. Prasad and H. C. A. Murthy, *ACS Omega*, 2023, **8**, 9597–9606.

21 A. Muzakki, H. Shabrany and R. Saleh, *The 3rd International Conference On Advanced Materials Science And Technology (Icamst)*, 2016, vol. 1725, p. 020051.

22 S. Kuld, M. Thorhauge, H. Falsig, C. F. Elkjaer, S. Helvig, I. Chorkendorff and J. Sehested, *Science*, 2016, **352**, 969–974.

23 A. Beck, M. A. Newton, M. Zabilskiy, P. Rzepka, M. G. Willinger and J. A. van Bokhoven, *Angew. Chem., Int. Ed.*, 2022, **61**, e202200301.

24 J. A. Montero, T. Welearegay, H. Stopfel, T. Dedova, I. O. Acik and L. Österlund, *RCS Adv.*, 2021, **11**, 10224.

25 M. Okazaki, Y. A. Wang, T. Yokoi and K. Maeda, *J. Phys. Chem. C*, 2019, **123**, 10429–10434.

26 T. Butburee, K. Papasara, P. Hirunsit, Z. Sun, Q. Tang, P. Khemthong, W. Sangkhun, W. Thongsuwan, P. Kumnorkaew, H. Wang and K. Faungnawkij, *J. Mater. Chem. A*, 2019, **7**, 8156.

27 L. Clarizia, G. Vitiello, R. B. Vadell, J. Sa, R. Marotta, I. D. Somma, R. Andreozzi and G. Luciani, *Int. J. Mol. Sci.*, 2023, **24**, 2004.

28 G. Wu, N. Guan and L. Li, *Catal. Sci. Technol.*, 2011, **1**, 601–608.

29 S. S. Djokic and L. Magagnin, *Metallization of semiconductors and nonconductive surfaces from aqueous solutions*, Springer, New York, 2014.

30 T. Baran, A. Visivile, M. Busch, X. He, S. Wojtyla, S. Rondinini, A. Minguzzi and A. Vertova, *Molecules*, 2021, **26**, 7271.

31 P. Venev, B. I. Stefanov, V. Milusheva, B. Tzaneva and V. Videkov, *Proc. 12th National Conference with International Participation "Electronica 2021"*, 2021.

32 B. I. Stefanov, V. Milusheva, H. G. Kolev and B. Tzaneva, *Catal. Sci. Technol.*, 2022, **13**, 7027.

33 M. A. Sliem, T. Hikov, Z. A. Li, M. Spasova, M. Farle, D. A. Schmidt, M. Havenith-Newen and R. A. Fischer, *Phys. Chem. Chem. Phys.*, 2010, **12**, 9858–9866.

34 Y. Chen, H. Zhao, B. Liu and H. Yang, *Appl. Catal., B*, 2015, **163**, 189–197.

35 G. Menagen, J. E. Macdonald, Y. Shemesh, I. Popov and U. Banin, *J. Am. Chem. Soc.*, 2009, **131**, 17406–17411.

36 M. Law, L. E. Greene, J. C. Johnson, R. Saykally and P. Yang, *Nat. Mater.*, 2005, **4**, 455–459.

37 N. S. McIntyre and M. G. Cook, *Anal. Chem.*, 1975, **47**, 2208–2213.

38 E. H. Park, J. Jung and H. H. Chung, *Chemosphere*, 2006, **64**, 432–436.

39 F. G. Svensson, E. Djurberg, S. Kim, G. Westin and L. Österlund, *Langmuir*, 2025, **41–42**, 28399–28410.

40 A. Kwiatkowski, J. Smulko, K. Drozdowska, L. Österlund and T. Welearegay, *Sol. Energy Mater. Sol. Cells*, 2024, **273**, 112940.

41 T. J. Frankcombe and Y. Liu, *Chem. Mater.*, 2023, **35**, 5468–5474.

42 M. Soltanmohammadi, E. Spurio, A. Gloystein, P. Luches and N. Nilius, *Phys. Status Solidi A*, 2023, **220**, 2200887.

43 N. Kumar, S. S. Parui, S. Limbu, D. K. Mahato, N. Tiwari and R. N. Chauhan, *Mater. Today: Proc.*, 2021, **41**, 237–241.

44 J. Thyr, J. Montero, L. Österlund and T. Edvinsson, *ACS Nanosci. Au*, 2021, **2**, 128–139.

45 J. Wang, X. M. Fan, D. Z. Wu, J. Dai, H. Liu, H. R. Liu and Z. W. Zhou, *Appl. Surf. Sci.*, 2011, **258**, 1797–1805.

46 M. I. Mahrsi, B. Chouchene, T. Gries, V. Carre, G. Medjahdi, F. Ayari, L. Balan and R. Schneider, *J. Environ. Chem. Eng.*, 2024, **12**, 113072.

47 A. Turki, C. Guillard, F. Dappozze, Z. Ksibi, G. Berhault and H. Kochkar, *Appl. Catal., B*, 2015, **163**, 404–414.

48 J. Fang, H. Fan, Y. Ma, Z. Wang and Q. Chang, *Appl. Surf. Sci.*, 2015, **332**, 47–54.

49 N. M. Flores, U. Pal, R. Galeazzi and A. Sandoval, *RSC Adv.*, 2014, **4**, 41099.

50 D. A. Giannakoudakis, J. A. Arcibar-Orozco and T. J. Bandosz, *Appl. Catal., B*, 2015, **174**, 96–104.